Temperature-Dependent Optical Properties of Gold Nanoparticles Coated with a Charged Diblock Copolymer and an Uncharged Triblock Copolymer

Sondre Volden,[†] Anna-Lena Kjøniksen,[‡] Kaizheng Zhu,[‡] Jan Genzer,[§] Bo Nyström,[‡] and Wilhelm R. Glomm[†,*]

[†]Ugelstad Laboratory, Department of Chemical Engineering, Norwegian University of Science and Technology (NTNU), N-7491 Trondheim, Norway, [‡]Department of Chemistry, University of Oslo, P.O. Box 1033, N-0315 Oslo, Norway, and [§]Department of Chemical and Biomolecular Engineering, North Carolina State University, Raleigh, North Carolina 27695

ABSTRACT We demonstrate that the optical properties of gold nanoparticles can be used to detect and follow stimuli-induced changes in adsorbed macromolecules. Specifically, we investigate thermal response of anionic diblock and uncharged triblock copolymers based on poly(*N*-isopropylacrylamide) (PNIPAAM) blocks adsorbed onto gold nanoparticles and planar gold surfaces in a temperature range between 25 and 60 °C. By employing a palette of analytical probes, including UV−visible spectroscopy, dynamic light scattering, fluorescence, and quartz crystal microbalance with dissipation monitoring, we establish that while the anionic copolymer forms monolayers at both low and high temperature, the neutral copolymer adsorbs as a monolayer at low temperatures and forms multilayers above the cloud point (T_C). Raising the temperature above T_C severely affects the optical properties of the gold particle/polymer composites, expelling associated water and altering the immediate surroundings of the gold nanoparticles. This effect, stronger for the uncharged polymer, is related to the amount of polymer adsorbed on the surface, where a denser shell influences the surface plasmon band to a greater degree. This is corroborated with light scattering experiments, which reveal that flocculation of the neutral polymer-coated particles occurs at high temperatures. The flocculation behavior of the neutral copolymer on planar gold surfaces results in multilayer formation. The observed effects are discussed within the framework of the Mie−Drude theory.

KEYWORDS: Mie−Drude · localized surface plasmon resonance · thermoresponsive NIPAAM polymers · ultraviolet spectroscopy · adsorption · dynamic light scattering · lower critical solution temperature

Over the past few years, functionalized gold (Au) nanoparticles have been implemented as versatile building blocks in microelectronics, catalysis, and biosensor applications (see *e.g.*, Shan *et al.* and references therein).[1] This activity is driven primarily by the intrinsic properties of Au in its particulate form, which displays a collective electron excitation of the conduction electrons known as a localized surface plasmon resonance (LSPR) band when irradiated by incident light.[1−3] Gold nanoparticles can be synthesized in diameters which span from the macroscopic (micrometers) down to the molecular scale (≈0.8 nm). Depending on the size, shape, and the extent of aggregation and dielectric function on the surface, the optical and electronic properties of the nanoparticles can be tuned considerably. To that end, the absorption maximum of the wavelength of the Au plasmon peak in UV−vis spectra, λ_{max}, can be shifted by hundreds of nanometers and particle charging energies can be altered by hundreds of millivolts by adjusting particle size and shape.[2,4] Because the surface chemistry of Au nanoparticles is similar to that of bulk Au, straightforward chemical routes involving deposition of self-assembled layers of both small as well as large organic molecules are possible.[5]

Stimuli-responsive polymers/copolymers, which undergo phase transitions in response to environmental stimuli, that is, temperature or pH, are characterized by a sharp coil-to-globule transition and subsequent phase separation above its lower critical solution temperature (LCST) in water. The LCST of thermally sensitive polymers can be tuned to a desired temperature range by adding different amounts of ionic surfactants.[6] Alternatively, it is also possible to alter the LCST of the polymer by copolymerization with a more hydrophilic (thus elevating the LCST) or a more hydrophobic (thus lowering the LCST) monomer. Poly(*N*-isopropylacrylamide) (PNIPAAM) is among the most extensively studied thermoresponsive polymers; it holds promising potential for drug delivery applications, separation, cell immobilization, gene transfection, diagnostics, and

*Address correspondence to glomm@nt.ntnu.no.

Received for review October 29, 2009 and accepted January 08, 2010.

Published online January 15, 2010. 10.1021/nn901517u

Methoxy-poly(ethylene glycol)-block-poly(N-isopropylacrylamide)- block- poly(methyl methacrylate) ($MPEG_{53}$-*b*-$P(NIPAAM)_{60}$-*b*-$P(MMA)_3$)

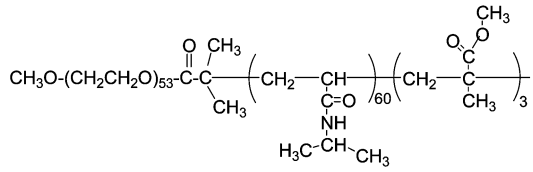

M_w = 13 400 g/mol; M_w/M_n = 1.07

Poly(*N*-isopropylacrylamide)-block-poly(3-sulfopropyl methacrylate potassium) ($P(NIPAAM)_{40}$-*b*-$P(SPMA)_5$)

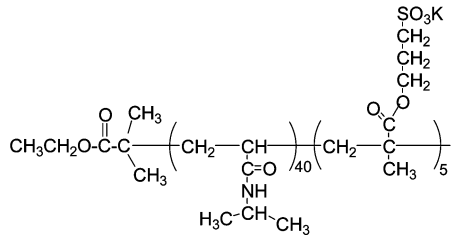

M_w = 5 900 g/mol; M_w/M_n = 1.09

Figure 1. Chemical structures, molecular weights, and polydispersities of the thermoresponsive charged diblock copolymer ($P(NIPAAM)_{40}$-*b*-$P(SPMA)_5$) and uncharged triblock ($MPEG_{53}$-*b*-$P(NIPAAM)_{60}$-*b*-$P(MMA)_3$) copolymer applied in this study.

other bioconjugation processes.[7−11] By copolymerizing NIPAAM with a pH-sensitive monomer, a triggering of phase separation by pH changes at specific temperatures can be achieved. This phenomenon may be employed in diagnostics or drug delivery applications as the chemical and physical properties of diseased tissue or tumors often differ from the surrounding environment (see, *e.g.*, review by Ganta[12] and references therein). For practical applications in medicine, it is desirable to involve species that display no unwanted cytotoxicity and which can be monitored readily throughout the target tissues.

Both in their own merit, as biomarkers and as carrying vessels, Au-polymer constructs are regarded as a promising new class of materials.[1,2] Au nanoparticles themselves offer a suitable scaffold onto which specific functionalities can be imparted, thus opening up new possibilities to tune the surface properties in any desired direction regarding, for example, wettability or direct biological effects. Additionally, Au colloids also possess certain desirable intrinsic physical properties such as optical labeling, thermal conductivity, and tunable size distributions. These qualities impart the metallic particles themselves with attractive biorelated effects, such as directed cytotoxicity, through either localized heat increases from excitation of the plasmon band[13] or by stimuli-triggered changes in physicochemical behavior of the colloidal constructs.[1,3] The optical signature of Au also allows it to be detected routinely in small amounts in tissues and cells. By combining Au colloids and thermoresponsive polymers, a system emerges that can adsorb and/or release entrapped molecules through temperature changes in the surroundings.

The chemical structures of polymers employed in this study are depicted in Figure 1, together with their weight-average molecular weights and polydispersity indexes. It should be noted that the experimentally determined cloud points were found to be concentration dependent.

We demonstrate in this paper that it is possible to tune the amount of adsorbed mass, the layer thickness, and the formation of mono- *versus* multilayers through varying the deposition temperature and by incorporating charged groups on the polymer. This can be taken advantage of in developing responsive colloidal materials with discrete size distributions, together with desired surface characteristics and labeling properties. The density of deposited layers can be manipulated through temperature variation, thereby allowing alterations in optical properties of Au-polymer constructs. The aim of this work is to examine the adsorption behavior of temperature-sensitive uncharged and charged copolymers on flat and convex citrate-covered Au surfaces in order to understand how the adsorption and absorption features can be modulated. We will demonstrate novel findings for copolymers containing PNIPAAM blocks and discuss how temperature-induced changes in the optical signature of Au nanoparticles can be used to detect transitions in the adsorbed polymer layer. More specifically, our findings demonstrate and open up the possibility of using the optical signature of plasmonic nanomaterials for tracking of environmentally induced changes in immobilized macromol-

ecules which has potential interest within a broad range of nanoscience applications.

RESULTS AND DISCUSSION

We used two derivatives of PNIPAAM polymers (Figure 1) for the temperature-ramped experiments; one uncharged triblock copolymer ($MPEG_{53}$-*b*-$P(NIPAAM)_{60}$-*b*-$P(MMA)_3$) and one charged diblock copolymer containing sulfonate groups ($P(NIPAAM)_{40}$-*b*-$P(SPMA)_5$). To gain a better understanding of the intermolecular interactions and insight into possible multilayer formation, experiments were also carried out on the charged polymer−Au conjugates to which a europium (Eu) salt was added to the suspension. The choice of salt stems both from the desire to incorporate a cation with high valency, enabling multiple associations with the charged polymer, combined with the fluorescent properties of Eu, allowing for detection in the micromolar range and below as well as probing of the local environment.

Figure 2 shows temperature dependencies of the apparent hydrodynamic radii (R_h) for the bulk solutions (0.082 wt %) of the copolymers without particles, which provides information about the temperature response of these polymers and their intrinsic ability to associate at higher temperatures. The correlation function for the solution of the charged diblock copolymer can be described by a single stretched exponential, and this mode is diffusive. From the Stokes−Einstein relationship the hydrodynamic radius can be calculated (see the experimental section). The value of R_h is only weakly temperature-dependent for the $P(NIPAAM)_{40}$-*b*-$P(SPMA)_5$ at this polymer concentration and over the considered temperature interval. This behavior reveals that most of the enhanced hydrophobicity of PNIPAAM at elevated temperatures is counteracted by the charges of the polymer. The high values of R_h observed for this polymer indicate that intermicellar complexes are formed at all temperatures employed. In the case of the uncharged triblock copolymer, two diffusive relaxation modes appear in the analysis of the correlation function and the hydrodynamic radii of species of different size are probed. The fast mode ($R_{h,f}$) pertains to the temperature-induced self-assembly of unimers to micelles and intermicellar structures, whereas the slow mode ($R_{h,s}$) depicts the growth of intermicellar complexes. The dilute solution of the uncharged triblock copolymer contains unimers, micelles, and intermicellar structures at low temperatures. As the temperature increases, the fraction of unimers is strongly reduced as the hydrophobicity of the polymer rises. At this stage, the populations of micelles and larger structures prevail.

Adsorption Properties of Solutions of $P(NIPAAM)_{40}$-*b*-$P(SPMA)_5$ and $MPEG_{53}$-*b*-$P(NIPAAM)_{60}$-*b*-$P(MMA)_3$ onto Planar Gold Surfaces. Adsorption experiments were conducted on a QCM to assess how the different polymers adsorb and orient themselves on a planar Au surface at various temperatures. Table 1 lists the mass adsorbed and thickness of the polymer layer. Also, the adsorption isotherms exhibit differences, where $P(NIPAAM)_{40}$-*b*-$P(SPMA)_5$ at 25 °C and $MPEG_{53}$-*b*-$P(NIPAAM)_{60}$-*b*-$P(MMA)_3$ at both 25 and 50 °C adsorb rapidly and nonreversibly, while $MPEG_{53}$-*b*-$P(NIPAAM)_{60}$-*b*-$P(MMA)_3$ at 50 °C displays slower adsorption kinetics (Figure 3).

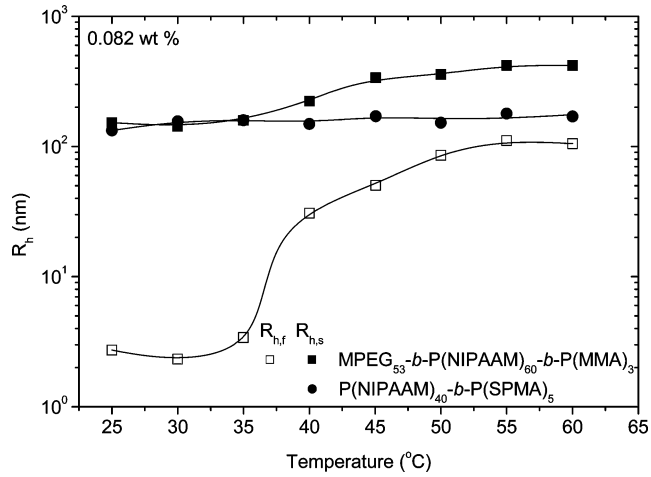

Figure 2. Temperature dependencies of the apparent hydrodynamic radii for polymer solutions (0.082 wt %) without particles (□ = $R_{h,f}$, ■, ● = $R_{h,s}$).

By comparing adsorption at ambient and elevated temperatures, the uncharged polymer adsorbs as a monolayer at the lower temperature applied, while at higher temperatures multilayers start forming. The charged polymer exhibits no difference in adsorption behavior between the two temperatures, giving rise to monolayers in both cases. Also worth noting is the fact that $P(NIPAAM)_{40}$-*b*-$P(SPMA)_5$ adsorbs to a lesser extent than $MPEG_{53}$-*b*-$P(NIPAAM)_{60}$-*b*-$P(MMA)_3$ with lower mass adsorbed and in thinner layers, likely due to charge repulsion between the anionic polymer and the citrate layer on the Au surface. The charges on the polymer will also reduce the tendency of the chains to form multilayers at elevated temperatures. It should however be noted that from these results it is not possible to rule out formation of incomplete monolayers, the main point is the temperature-induced differences in adsorption behavior causing layers of varying thickness to form. This temperature-dependent layer formation can be taken advantage of as demonstrated in the following section.

TABLE 1. Polymer Adsorption on Planar Gold Surfaces, as Measured by QCM-D

sample	temperature (°C)	mass adsorbed (ng/cm²)	layer thickness (nm)	
$MPEG_{53}$-*b*-$P(NIPAAM)_{60}$-*b*-$P(MMA)_3$	25	350 ± 41	5 ± 1	monolayer
	50	849 ± 145	13 ± 3	multilayer
$P(NIPAAM)_{40}$-*b*-$P(SPMA)_5$	25	142 ± 4	1.65 ± 0.07	monolayer
	50	149 ± 10	3.3 ± 0.6	monolayer

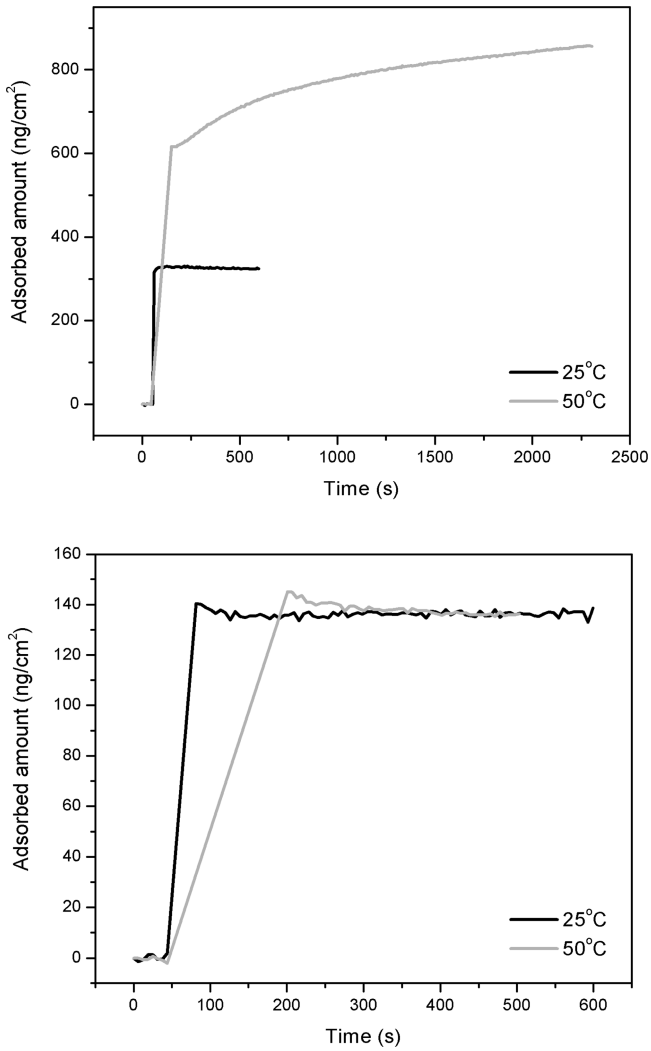

Figure 3. Effect of temperature on adsorbed mass of $MPEG_{53}$-*b*-$P(NIPAAM)_{60}$-*b*-$P(MMA)_3$ (upper panel) and $P(NIPAAM)_{40}$-*b*-$P(SPMA)_5$ (lower panel) on planar citrate-covered gold surfaces as a function of time, as determined at a bulk concentration of 0.02 wt % by QCM-D.

Adsorption of the Copolymers onto Au Nanoparticles. The zeta-potentials and particle sizes measured for Au nanoparticles covered with either a citrate layer or coated with polymer are listed in Table 2. The citrate groups present on the particles surfaces are supplied during the synthesis of these particles and act as stabilizers preventing the nanoparticles from aggregating and precipitating. The particle surface charge is eliminated upon adsorption of the copolymers onto the particles. Both solutions are stable for long periods of time after being coated with polymer, revealing that the adsorbed macromolecules impart a steric stabilization to these systems. The fact that the zeta-potential is approximately zero also for Au nanoparticles with adsorbed charged copolymer suggests that the charge density is low. The particle size assessed by means of light scattering (see also discussion below) increases when polymer is adsorbed, with $MPEG_{53}$-*b*-$P(NIPAAM)_{60}$-*b*-$P(MMA)_3$ yielding a thicker layer, in line with the QCM-D results.

Figure 4 illustrates the temperature dependencies of the turbidity for the two copolymers at the concentrations of 0.016 wt % (a) and 0.082 wt % (b) in the following systems: polymer−Eu^{3+}, polymer−Au, and polymer−Au−Eu^{3+}. For the $P(NIPAAM)_{40}$-*b*-$P(SPMA)_5$ system, the turbidity is very low and virtually independent of temperature and the composition of the system. The turbidity of solutions containing $MPEG_{53}$-*b*-$P(NIPAAM)_{60}$-*b*-$P(MMA)_3$ exhibit an upturn at elevated temperatures. The increase in turbidity commences at ≈45 °C for all the solutions containing $MPEG_{53}$-*b*-$P(NIPAAM)_{60}$-*b*-$P(MMA)_3$, but it is most pronounced for the highest polymer concentration, and for the $MPEG_{53}$-*b*-$P(NIPAAM)_{60}$-*b*-$P(MMA)_3$−Au−Eu^{3+} system at the lowest polymer concentration. This upturn reflects the enhanced hydrophobicity of PNIPAAM at high temperatures, leading to the formation of large aggregates. The system $MPEG_{53}$-*b*-$P(NIPAAM)_{60}$-*b*-$P(MMA)_3$−Au−Eu^{3+} maintains the highest turbidity values over the whole temperature range, and for the highest polymer concentration. This system is much more turbid than the $MPEG_{53}$-*b*-$P(NIPAAM)_{60}$-*b*-$P(MMA)_3$−Eu^{3+} and $MPEG_{53}$-*b*-$P(NIPAAM)_{60}$-*b*-$P(MMA)_3$−Au solutions, which suggests that the presence of Eu^{3+} ions enhances the interactions between $MPEG_{53}$-*b*-$P(NIPAAM)_{60}$-*b*-$P(MMA)_3$ and the Au-nanoparticles.

Figure 5 shows the hydrodynamic radius (R_h) determined from the DLS measurements. R_h for the samples containing $P(NIPAAM)_{40}$-*b*-$P(SPMA)_5$ (Figure 5 panels c and d) is, in accordance with the turbidity data, nearly temperature independent. For the highest polymer concentration (Figure 5d), the sizes of $P(NIPAAM)_{40}$-*b*-$P(SPMA)_5$−Au particles and the $P(NIPAAM)_{40}$-*b*-$P(SPMA)_5$−Au−Eu^{3+} complexes are very close to the value of R_h for the pure Au nanoparticles (represented by the horizontal lines in Figure 5), indicating that relatively little polymer is adsorbed on the surface of the Au particles. This result is in agreement with the QCM results (Table 1), which reveal that $P(NIPAAM)_{40}$-*b*-$P(SPMA)_5$ forms monolayers at both 25 and 50 °C. Since the Au nanoparticles have much higher scattered intensity than free $P(NIPAAM)_{40}$-*b*-$P(SPMA)_5$ in water, only the Au nanoparticles with and without adsorbed polymer are probed by the correlation functions when Au is present in the samples. When there is no Au present in the $P(NIPAAM)_{40}$-*b*-$P(SPMA)_5$ system the measured R_h is more than 100 nm, indicating that large aggregates are formed. A close examination of the DLS curves re-

TABLE 2. Zeta-Potentials and Hydrodynamic Radii for Bare Au Nanoparticles and Polymer Covered Au Particles

	ζ-potential (mV)	R_h (nm)
Au 30 nm w/citrate layer	−41.1 ± 0.1	14.8 ± 0.1
Au 30 nm with $MPEG_{53}$-*b*-$P(NIPAAM)_{60}$-*b*-$P(MMA)_3$	≈ 0	16.3 ± 0.1
Au 30 nm with $P(NIPAAM)_{40}$-*b*-$P(SPMA)_5$	≈ 0	15.8 ± 0.1

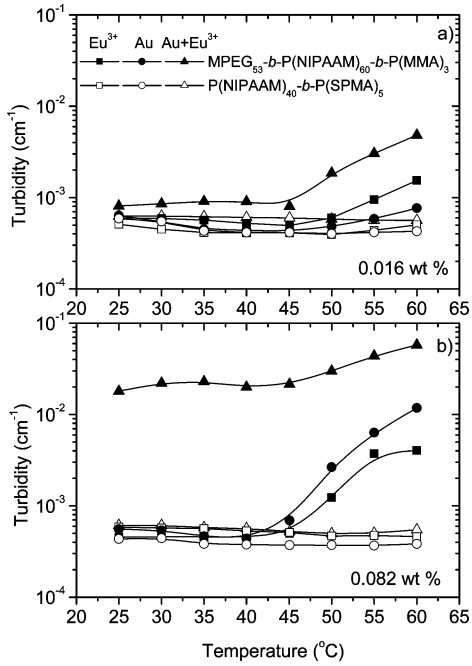

Figure 4. Temperature dependencies of the turbidity for the indicated concentrations of the polymers $MPEG_{53}$-*b*-$P(NIPAAM)_{60}$-*b*-$P(MMA)_3$ and $P(NIPAAM)_{40}$-*b*-$P(SPMA)_5$ in the presence of europium and for the systems polymer−Au and polymer−Au−Eu^{3+}.

veals that the sizes of these aggregates increase slightly with temperature due to the enhanced hydrophobicity of the PNIPAAM groups. The addition of Eu^{3+} screens out some of the charges in the system, resulting in a contraction of the aggregates, and a slightly lower hydrodynamic radius. Even though the aggregates are very large, both the scattered intensity from the DLS measurements (not shown) and the turbidity values (Figure 4) are very low, indicating that the aggregates possess a relatively open structure due to the electrostatic repulsion between the charged SPMA groups. The low scattering intensity results in very poor correlation functions; it is therefore not possible to analyze the correlation functions at the lowest polymer concentration in the absence of Au, and for $P(NIPAAM)_{40}$-*b*-$P(SPMA)_5$−Eu^{3+} for the highest polymer concentration at low temperatures.

Interestingly, at the lowest $P(NIPAAM)_{40}$-*b*-$P(SPMA)_5$ concentration (Figure 5c), the $P(NIPAAM)_{40}$-*b*-$P(SPMA)_5$−Au−Eu^{3+} sample yields larger values of R_h than what is observed for $P(NIPAAM)_{40}$-*b*-$P(SPMA)_5$−Au (at either concentration) and for $P(NIPAAM)_{40}$-*b*-$P(SPMA)_5$−Au−Eu^{3+} at the high concentration. The higher values of R_h indicate that at this low polymer concentration and in the presence of Eu^{3+}, there is a significant adsorption (probably multilayers) of $P(NIPAAM)_{40}$-*b*-$P(SPMA)_5$ onto the Au nanoparticles. In the absence of salt, both $P(NIPAAM)_{40}$-*b*-$P(SPMA)_5$ and the Au nanoparticles contain negative charges, and the repulsive forces prevent large amounts of this polymer to be adsorbed to the Au surface. When Eu^{3+} is added to the samples at the lowest polymer concentration, the salt screens out most of the electrostatic repulsive forces, and the polymer can easily adsorb to the Au surface. However, at the higher polymer concentration, the amount of Eu^{3+} present in the sample is not high enough to screen out all the electrostatic interactions. As a result, the system behaves similar to what is observed in the absence of Eu^{3+}.

In specimens containing $MPEG_{53}$-*b*-$P(NIPAAM)_{60}$-*b*-$P(MMA)_3$ (Figure 5a,b), R_h increases at temperatures above 45 °C due to the enhanced hydrophobicity of PNIPAAM at elevated temperatures. This is in accordance with the turbidity upturn observed at high temperatures for the same systems. For both concentrations, R_h of $MPEG_{53}$-*b*-$P(NIPAAM)_{60}$-*b*-$P(MMA)_3$−Au is close to that of the bare Au nanoparticles at low temperatures, indicating that the amount of polymer adsorbed on the Au particles is low. At higher temperatures, R_h is much larger than for the bare Au nanoparticles, suggesting the formation of polymer multilayers and possibly large aggregates containing a combination of Au nanoparticles and $MPEG_{53}$-*b*-$P(NIPAAM)_{60}$-*b*-$P(MMA)_3$. This confirms the results from QCM (Table 1) which reveal that for $MPEG_{53}$-*b*-$P(NIPAAM)_{60}$-*b*-$P(MMA)_3$ monolayers are formed at 25 °C, whereas multilayers are formed at 50 °C.

In accord with the turbidity results (Figure 4), the hydrodynamic radius of $MPEG_{53}$-*b*-$P(NIPAAM)_{60}$-*b*-$P(MMA)_3$−Au−Eu^{3+} is significantly higher than what is observed for $MPEG_{53}$-*b*-$P(NIPAAM)_{60}$-*b*-$P(MMA)_3$−Au for both polymer concentrations and over the whole temperature range. For the lowest polymer concentration (Figure 5a), the scattered intensity of $MPEG_{53}$-*b*-$P(NIPAAM)_{60}$-*b*-$P(MMA)_3$ in pure water is too low to obtain usable correlation functions. The same applies for $MPEG_{53}$-*b*-$P(NIPAAM)_{60}$-*b*-$P(MMA)_3$−Eu^{3+} at low tem-

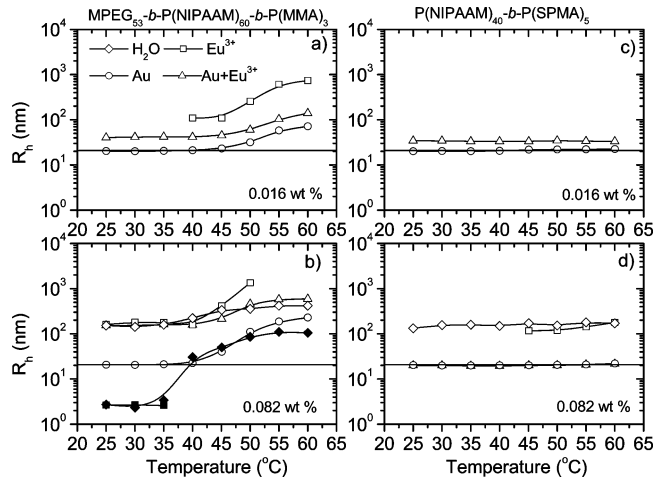

Figure 5. Temperature dependencies of the apparent hydrodynamic radii (from DLS) for the indicated systems and polymer concentrations. The solid horizontal lines represent the size of the pure gold nanoparticles without any polymer present. Solid symbols represent the radius calculated from the fast mode (analogous open and closed symbols represent the same system).

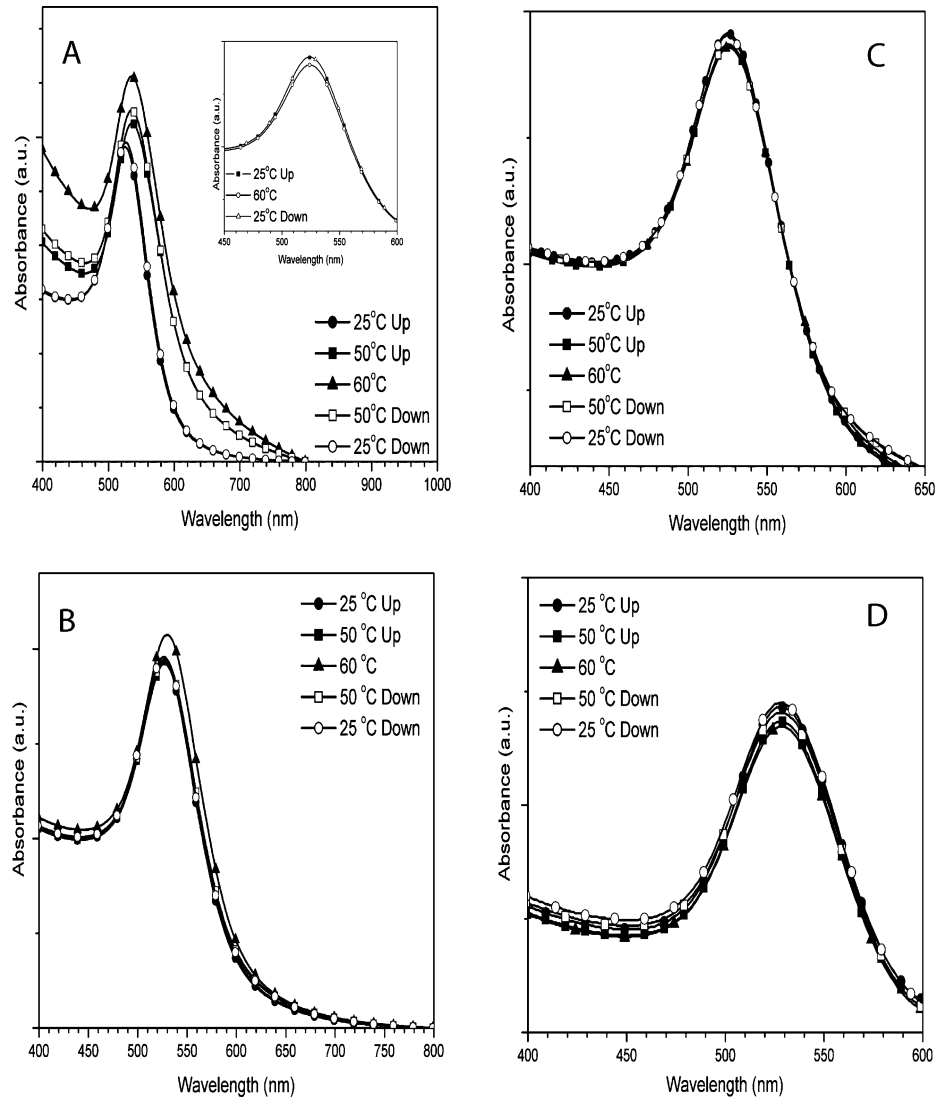

Figure 6. Temperature-induced absorbance shifts for 30 nm Au particles coated with excess (0.082 wt %) $MPEG_{53}$-*b*-$P(NIPAAM)_{60}$-*b*-$P(MMA)_3$ (A) and a centrifuged and resuspended sample (B). The inset in panel A shows the temperature induced changes for bare Au particles. UV-spectra for Au particles with excess (0.082 wt %) $P(NIPAAM)_{40}$-*b*-$P(SPMA)_5$ (C) and a resuspended sample (D) are also shown. The term "Up" refers to the heating part of the temperature loop, "Down" refers to the cooling down cycle of the experiment.

peratures. At the temperatures where the latter can be analyzed, R_h of $MPEG_{53}$-*b*-$P(NIPAAM)_{60}$-*b*-$P(MMA)_3-Au-Eu^{3+}$ is much lower than what is observed for $MPEG_{53}$-*b*-$P(NIPAAM)_{60}$-*b*-$P(MMA)_3-Eu^{3+}$. However, both the scattered intensity from DLS (not shown) and the turbidity (Figure 4a) is higher for $MPEG_{53}$-*b*-$P(NIPAAM)_{60}$-*b*-$P(MMA)_3-Au-Eu^{3+}$ than for $MPEG_{53}$-*b*-$P(NIPAAM)_{60}$-*b*-$P(MMA)_3-Eu^{3+}$. This indicates that Au nanoparticles with adsorbed polymer are probed by the correlation functions, and multilayers and large Au−polymer aggregates form in the 0.016 wt % $MPEG_{53}$-*b*-$P(NIPAAM)_{60}$-*b*-$P(MMA)_3-Au-Eu^{3+}$ samples.

As mentioned in the discussion regarding Figure 2, the correlation function for 0.082 wt % solutions of $MPEG_{53}$-*b*-$P(NIPAAM)_{60}$-*b*-$P(MMA)_3$ exhibits two relaxation modes. The same behavior is also observed for the $MPEG_{53}$-*b*-$P(NIPAAM)_{60}$-*b*-$P(MMA)_3-Eu^{3+}$ system at the same polymer concentration, but only at temperatures below 40 °C. As the temperature is increased, $MPEG_{53}$-*b*-$P(NIPAAM)_{60}$-*b*-$P(MMA)_3-Eu^{3+}$ grows larger than the pure polymer in water and only one relaxation mode is evident in the relaxation mode, indicating that there is a salting out effect of the polymer at elevated temperatures where the hydrophobicity of PNIPAAM prevails. At temperatures above 50 °C, multiple scattering is found for this system thus precluding the analysis of the correlation functions. At this polymer concentration and at low temperatures, R_h of $MPEG_{53}$-*b*-$P(NIPAAM)_{60}$-*b*-$P(MMA)_3-Au-Eu^{3+}$ is similar to that of the large aggregates detected for $MPEG_{53}$-*b*-$P(NIPAAM)_{60}$-*b*-$P(MMA)_3$ in water and for the $MPEG_{53}$-*b*-$P(NIPAAM)_{60}$-*b*-$P(MMA)_3-Eu^{3+}$ system. However, as was observed for the low polymer concentration, the scattered intensity from DLS (not shown) and the turbidity (Figure 4b) is higher for $MPEG_{53}$-*b*-$P(NIPAAM)_{60}$-*b*-

$P(MMA)_3$—Au—Eu^{3+}, and only one relaxation mode is detected for this system. The conjecture is that large aggregates containing $MPEG_{53}$-*b*-$P(NIPAAM)_{60}$-*b*-$P(MMA)_3$ and Au nanoparticles are formed in the presence of Eu^{3+}. The salting out of the polymer, giving poorer thermodynamic conditions in the presence of Eu^{3+}, combined with the salt-induced screening of some of the charges on the Au nanoparticles, which renders them more hydrophobic, gives rise to the enhanced interactions between $MPEG_{53}$-*b*-$P(NIPAAM)_{60}$-*b*-$P(MMA)_3$ and the Au particles in the presence of Eu^{3+}.

Temperature-Dependent Optical Properties of Gold Particles Covered with $MPEG_{53}$-*b*-$P(NIPAAM)_{60}$-*b*-$P(MMA)_3$ or $P(NIPAAM)_{40}$-*b*-$P(SPMA)_5$. Figure 6 displays the heating and cooling cycles on the absorbance spectra for Au nanoparticles with $MPEG_{53}$-*b*-$P(NIPAAM)_{60}$-*b*-$P(MMA)_3$ and $P(NIPAAM)_{40}$-*b*-$P(SPMA)_5$. In the presence of excess of $MPEG_{53}$-*b*-$P(NIPAAM)_{60}$-*b*-$P(MMA)_3$ (0.082 wt %, Figure 6A) and after centrifugation (Figure 6B), both spectra display a bathochromic shift (red-shift) of the LSPR peak upon increasing the temperature, as well as an increased absorbance, before gradually returning to the initial values upon cooling. No major line shape changes occur upon heating and cooling of the samples. This trend is more pronounced when the polymer is present in excess than for the washed and resuspended samples (*cf.* Figure 6). For Au nanoparticle solutions containing excess amounts of $P(NIPAAM)_{40}$-*b*-$P(SPMA)_5$ (0.082 wt %, Figure 6C) and a centrifuged and resuspended sample (Figure 6D) both the shifts in λ_{max} (hereafter referred to as λ_{LSPR}) and in intensity are less pronounced than in the case of $MPEG_{53}$-*b*-$P(NIPAAM)_{60}$-*b*-$P(MMA)_3$-covered particles. The intensity decreases slightly upon heating before returning to their initial values when cooling down.

Figure 7 displays the LSPR peak positions as a function of temperature for the $MPEG_{53}$-*b*-$P(NIPAAM)_{60}$-*b*-$P(MMA)_3$—Au and $P(NIPAAM)_{40}$-*b*-$P(SPMA)_5$—Au nanoparticles, with the corresponding data for bare (*i.e.*, citrate-coated) Au nanoparticles in the absence of polymer included for comparison. A summary of UV—vis data is provided in Table 3. The entirety of the polymer—Au nanoparticle constructs studied display a slight red-shift of the LSPR compared to bare Au nanoparticles, indicating a change of the dielectric function on the surface from adsorption of polymer. For $P(NIPAAM)_{40}$-*b*-$P(SPMA)_5$ the centrifuged counterpart is significantly red-shifted relative to the sample with excess polymer (Figure 7, Table 3), where the 0.016% and the 0.082% samples completely overlap one another. Results for the uncharged polymer show similar trends upon heating and cooling, with a red-shift of the LSPR peak position upon heating. For $MPEG_{53}$-*b*-$P(NIPAAM)_{60}$-*b*-$P(MMA)_3$—Au, the centrifuged samples display much smaller bathochromic shifts relative to samples with excess polymer, revealing that the excess polymer plays a significant role in the thermoresponsive optical behavior of these colloidal assemblies. This temperature-dependent shift of the LSPR peak position is not visible for the unmodified colloids. Another char-

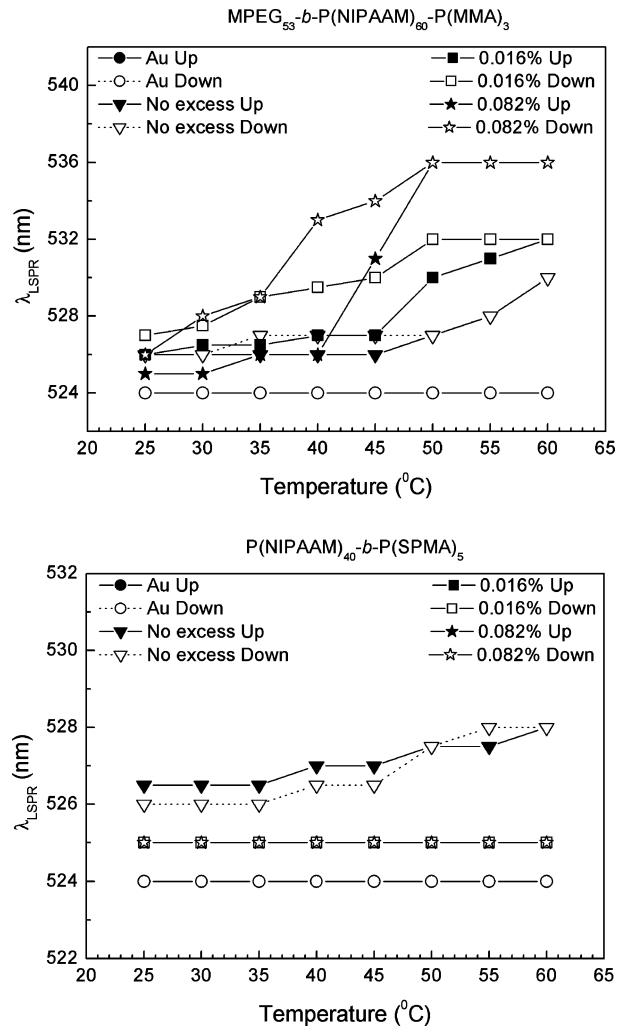

Figure 7. Shift in the localized surface plasmon resonance (LSPR) as a function of temperature for $MPEG_{53}$-*b*-$P(NIPAAM)_{60}$-*b*-$P(MMA)_3$—Au (top panel) and $P(NIPAAM)_{40}$-*b*-$P(SPMA)_5$—Au (bottom panel). "Up" denotes the heating process while "Down" refers to the cooling process. "No excess" is used for the centrifugated and resuspended sample.

TABLE 3. UV-Visible Absorption Data for Polymer—Au Constructs

sample	[polymer] (wt %)	λ_{LSPR} (nm) at 25 °C	$\Delta\lambda_{LSPR}$ (nm) at 60 °C
Au sol		524	0
$MPEG_{53}$-*b*-	0.082	525	11
$P(NIPAAM)_{60}$-*b*-	0.016	526	5
$P(MMA)_3$	centrifuged	526	5
	0.082	525	0
$P(NIPAAM)_{40}$-*b*-	0.016	526	0
$P(SPMA)_5$	centrifuged	526	2
$MPEG_{53}$-*b*-$P(NIPAAM)_{60}$-*b*-$P(MMA)_3$ + Eu^{3+}	0.082	550	
$P(NIPAAM)_{40}$-*b*-$P(SPMA)_5$ + Eu^{3+}	0.082	536	1

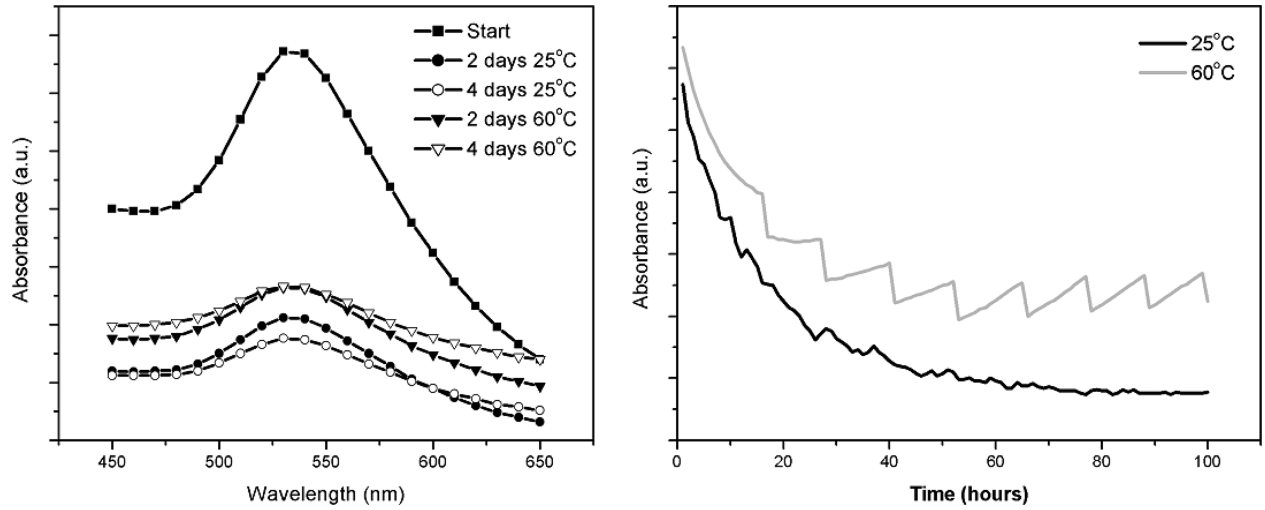

Figure 8. UV−vis absorbance spectra for Eu^{3+}-induced precipitation of $P(NIPAAM)_{40}$-*b*-$P(SPMA)_5$-coated Au nanoparticles at 25 and 60 °C (left panel), and time induced loss of absorption intensity at λ = 535 nm (right panel).

acteristic feature of $MPEG_{53}$-*b*-$P(NIPAAM)_{60}$-*b*-$P(MMA)_3$−Au and $P(NIPAAM)_{40}$-*b*-$P(SPMA)_5$−Au systems is the presence of a hysteresis loop between the heating and cooling sequences (Figure 7). For $MPEG_{53}$-*b*-$P(NIPAAM)_{60}$-*b*-$P(MMA)_3$−Au, this hysteresis occurs between 50 and 25 °C for the sample with an excess of polymer and between 50 and 30 °C for the washed and resuspended sample, before returning to the initial states upon completion of the temperature loop (sample with excess polymer displays a difference of 1 nm of the LSPR between the initial sample and upon completion of the temperature cycle). The cause of the observed hysteresis might lie in a difference in adsorption and desorption rates where, as the temperature is raised, single molecules adhere to a growing shell layer in a sequential manner. As the temperature is lowered, the polymers are desorbed in small aggregates causing a more rapid decrease in the thickness of the passivating layer. For $P(NIPAAM)_{40}$-*b*-$P(SPMA)_5$ there are no distinct changes in the LSPR peak position when ramping the temperature except for the resuspended particles where a slight red-shift is observed for temperatures above 40 °C.

An interesting feature of the $P(NIPAAM)_{40}$-*b*-$P(SPMA)_5$−Au conjugate appears when the Eu salt is added (Figure 8). While the sol precipitation starts to level off after around 48 h, it can be resuspended easily by agitation or stirring. The time-induced loss of absorption intensity (Figure 8, right panel) is larger at low temperature than at elevated temperatures, which can be ascribed to increased thermal motion of the nanoparticles in the latter case. Also, the sawtooth-like appearance of the plot at 60 °C could be interpreted as emanating from varying proximity of the colloidal cores to each other. As these approach each other, the absorbance intensity might be increased due to driving off of the polymer layer at elevated temperatures, resulting in Au−Au contact and temporarily larger suspended particles/flocs. At regular intervals there is a sudden drop in intensity possibly caused by buildup of complexating agents between the particles (thus increasing the interparticle distance) or due to particles being precipitated from the bulk solution as their size exceed a certain threshold. Attempts to calculate a time constant for the precipitation derived from the data presented in the right panel of Figure 8 yielded an exponential decay of −0.28 for the low temperature precipitation and −0.17 for the high temperature. Calculations were performed after a trendline had been fitted to each of the curves. The results indicate a faster rate of precipitation at 25 °C, in a more level manner. Additionally, Eu itself causes a bathochromic shift of 10.5 nm relative to the polymer−nanoparticle complexes (*cf.* Table 3). This can be ascribed to a charge interaction between Eu^{3+} and sulfonate groups on the polymer leading to contraction of the polymer layer thereby altering the immediate surroundings of the Au particles. For the system with Eu^{3+} added, a hysteresis loop is also observed with respect to LSPR as a function of temperature.

The optical properties of Au and Ag nanoparticles in a given system are discussed typically within the framework of the Mie−Drude theory; for a theoretical treatment, see, for example, Franzen[14] or Mulvaney.[15−17] The Mie−Drude theory predicts the effect of particle size, interparticle distance, dielectric function of the surrounding medium, and core charge state on the LSPR absorption band of metal nanoparticles. The LSPR band of nanoparticles coated with a passivating layer of surfactants or polymers is also influenced by the thickness of the coating/shell layer, and the volume fraction (*g*) of the shell layer. Assuming that the size of the metal core is kept constant, a bathochromic shift of the LSPR is expected to occur (i) as the interparticle distance is reduced, (ii) with increasing the refractive index of the solvent ($\in_m = n_m^2$), (iii) with increasing the refractive in-

dex of the shell layer ($\in_s = n_s^2$), (iv) with increasing the thickness of the shell layer, as this will raise the volume fraction g of the shell, and (v) with an electron deficiency with respect to the point/potential of zero charge (E_{PZC}).

According to Collier *et al.*,[18,19] strong interparticle coupling and a concomitant red-shift occurs as the separation D between nanoparticles of radius r approaches a critical value of $D/(2r) = 1.2$. Although we cannot rule out the existence of weak interparticle coupling, this does not seem to be the primary mechanism behind the temperature-dependent spectral shifts of the LSPR observed in this study. The LSPR is red-shifted continually with increasing temperature; this shift is reversible upon cooling, as shown in Figures 6 and 7. Moreover, because the concentration of the Au nanoparticles is only ~0.3 nM and the reversibility is observed in the absence of any mechanical stirring, it is not likely that the suspensions studied here form such dense flocs as to satisfy the $D/(2r) = 1.2$ criterion. We thus do not consider mechanism (i) as described above to provide an adequate explanation for the observed spectral shifts. The refractive index of water decreases slightly (~0.55%[20]) from 25 to 70 degrees, which according to Mie−Drude theory, should cause a slight hypsochromic shift (blue-shift).[16] As the position of the LSPR band of citrate-coated Au nanoparticles is unaffected by temperature within the intervals studied here, we conclude that mechanism (ii), that is, changes in the dielectric function of the surrounding medium, is not responsible for the observed temperature-dependent spectral changes of the polymer-coated Au nanoparticles.

Mechanisms (iii) and (iv), the increase in the refractive index of the polymer shell and an increase in the volume fraction of the shell layer g, respectively, are likely to be the primary contributing factors to the observed shifts of the LSPR band for the polymer−Au nanoparticle constructs. With increasing temperature, the PNIPAAM chains contract, leading to a denser shell layer resulting in a red-shift.[21−23] Mechanism (iii) can also account for the reversibility of the LSPR shift, provided the contraction of PNIPAAM chains does not alter significantly the number of binding sites per polymer chain on the gold nanoparticle. Upon increasing the temperature, the red-shift is observed both when the polymer is present in excess and when the solutions have been washed and resuspended (not for all $P(NIPAAM)_{40}$-*b*-$P(SPMA)_5$−Au samples), although to a lesser extent for the sample without excess polymer, which suggests that mechanism (iii) does indeed play a major role in the spectral shifts of the LSPR band. In the presence of excess $MPEG_{53}$-*b*-$P(NIPAAM)_{60}$-*b*-$P(MMA)_3$, the shift of the LSPR band is more pronounced, which suggests that multilayers form on the particle surface upon increasing the temperature, thus increasing the volume fraction g of the shell layer. Upon decreasing the temperature, the hydrophobic interactions subside gradually, leading to desorption and a blue-shift of the LSPR band. This trend is much less pronounced for PNIPAAM with charged moieties, i.e., P(NIPAAM)-*b*-P(SPMA), which supports the hypothesis of formation of multilayers through hydrophobic interactions. Thus, our results indicate that mechanisms (iii) and (iv) both contribute to the absorption behavior of the polymer−Au nanoparticle constructs with an excess of polymer, while mechanism (iii) is the primary mechanism for the spectral shifts of the LSPR band observed for the samples without excess polymer. This conclusion is further supported by QCM data for adsorption of the polymers to planar surfaces. It should be noted that DLS results for the $MPEG_{53}$-*b*-$P(NIPAAM)_{60}$-*b*-$P(MMA)_3$−Au system disclose evolution of aggregates at elevated temperatures. This process is likely initiated by Au nanoparticles that are covered by a multilayer of the copolymer, and the flocs are created through hydrophobic interactions. For the $P(NIPAAM)_{40}$-*b*-$P(SPMA)_5$−Au system no temperature-induced aggregation could be detected.

For the charged polymer system with added Eu salt, the LSPR band is significantly red-shifted already at room temperature. This behavior can be accounted for by mechanism (v) defined above, wherein the Eu^{3+} ions penetrate the polymer shell and interact with the colloidal Au core, thus reducing the electronic charge at the Au surface. A comparative test was carried out with the $MPEG_{53}$-*b*-$P(NIPAAM)_{60}$-*b*-$P(MMA)_3$−Au conjugates to see if there was a similar shift in λ_{max} when the Eu salt was added. The absorption maximum at room temperature is shifted *ca.* 25 nm (*cf.* Table 3) indicating that the red-shift effect is caused by the Eu^{3+} being located sufficiently close to the core to induce a change in the surface charge density of the Au particles. Moreover, since the initial bathochromic shift is smaller for the Au particles coated with charged polymer, a part of the cations interact with the anionic groups on the polymer, hence being prevented from penetrating through to the surface. This notion is further confirmed by the kinetics of precipitation, where the uncharged polymer-coated Au particles precipitate at a higher rate.

Steady-State Fluorescence from $MPEG_{53}$-*b*-$P(NIPAAM)_{60}$-b-$P(MMA)_3$−Au and $P(NIPAAM)_{40}$-*b*-$P(SPMA)_5$−Au in the Presence of Eu(III). Steady-state emission spectra for $EuCl_3$ and for the systems $MPEG_{53}$-*b*-$P(NIPAAM)_{60}$-*b*-$P(MMA)_3$−Eu^{3+} and $MPEG_{53}$-*b*-$P(NIPAAM)_{60}$-*b*-$P(MMA)_3$−Au−Eu^{3+} at two different temperatures are shown in Figure 9. Spectra of Eu^{3+} alone at the two temperatures divulge that three emission bands can be distinguished: one broad-band centered at ~543 nm, one band centered at ~591 nm, and one band centered at ~615 nm.

The detected bands can, in descending order of frequency, be assigned as $^7F_2/^7F_1 \leftarrow {}^5D_1$ (~543 nm), $^7F_1 \leftarrow {}^5D_0$ (~591 nm) and $^7F_2 \leftarrow {}^5D_0$ (~615 nm).[24−26] While generally the band intensity in the Eu^{3+} spectra in-

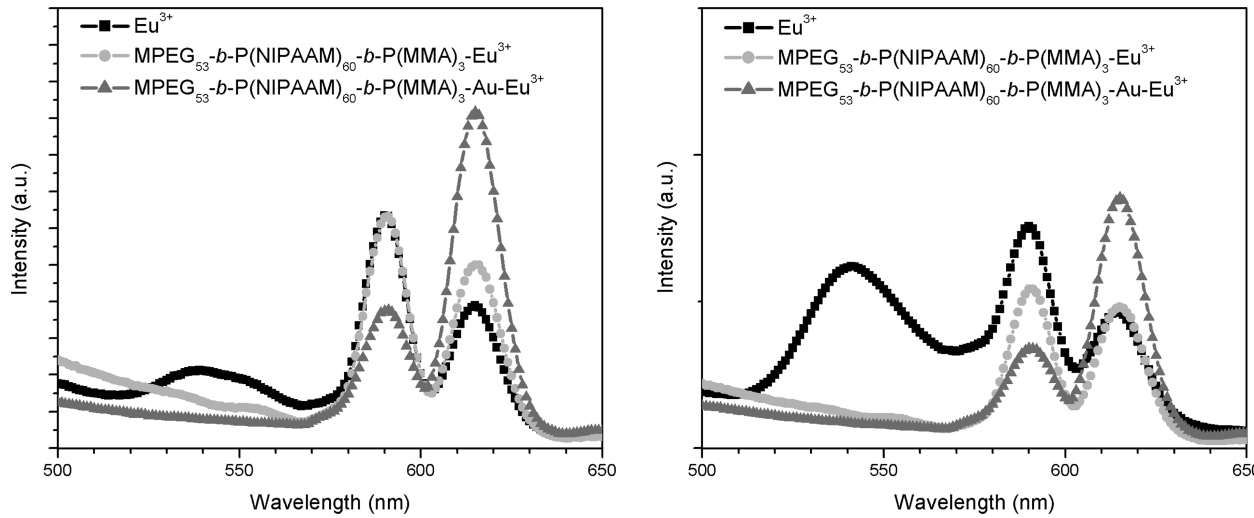

Figure 9. Steady-state fluorescence spectra for $EuCl_3$ and for the systems $MPEG_{53}$-*b*-$P(NIPAAM)_{60}$-*b*-$P(MMA)_3-Eu^{3+}$ and $MPEG_{53}$-*b*-$P(NIPAAM)_{60}$-*b*-$P(MMA)_3-Au-Eu^{3+}$ at two temperatures: 25 °C (left) and 50 °C (right). Excitation wavelength 405 nm.

creases with temperature, it does not return to the initial values upon completion of the temperature loop. Most likely this is caused by dehydration of crystalline water associated with Eu^{3+} as the temperature is raised. This feature is prominent especially for the $^7F_2/^7F_1 \leftarrow {}^5D_1$ transition, which is weak until heated above 30 °C, where it approaches the intensity of the other two transitions. The $^7F_1 \leftarrow {}^5D_0$ transition is relatively strong among the $^7F_J \leftarrow {}^5D_0$ transitions, largely independent of the ligand environment, and primarily magnetic dipole in character.[27] The characteristic "Eu red" $^7F_2 \leftarrow {}^5D_0$ (~615 nm) luminescence possesses a character of an essentially purely electric dipole, and the intensity is very sensitive to ligand structure, ligand field symmetry, and chemical environment.[26] Thus, the ratio between the $^7F_1 \leftarrow {}^5D_0$ and the $^7F_2 \leftarrow {}^5D_0$ transitions (hereafter referred to as the *m*/*e* ratio) provides a useful measure with which to gauge changes in the chemical environment of Eu^{3+}. For the aqueous solutions of Eu^{3+} studied here, the *m*/*e* ratio was found to be 1.6 (*cf.* Table 4).

Although the general features from the Eu^{3+} sample are retained in the emission spectra of $MPEG_{53}$-*b*-$P(NIPAAM)_{60}$-*b*-$P(MMA)_3-Eu^{3+}$ (Figure 9), the $^7F_2/^7F_1 \leftarrow {}^5D_1$ (~543 nm) transition is less prominent. Moreover, the overall emission intensity of Eu^{3+} is notably (>25%) reduced compared to the solution with only Eu^{3+}. This is to be expected, as acrylamide is used commonly as a fluorescence quencher.[28] The *m*/*e* ratio for the $MPEG_{53}$-*b*-$P(NIPAAM)_{60}$-*b*-$P(MMA)_3-Eu^{3+}$ system is reduced from 1.6 (Eu^{3+} only) to 1.3 (*cf.* Table 4), indicating interaction between the polymer and Eu^{3+}. Figure 9 also depicts the behavior of the $MPEG_{53}$-*b*-$P(NIPAAM)_{60}$-*b*-$P(MMA)_3-Eu^{3+}$ system in the presence of Au nanoparticles, where the emission intensity of the $MPEG_{53}$-*b*-$P(NIPAAM)_{60}$-*b*-$P(MMA)_3-Au-Eu^{3+}$ system is further reduced relative to Eu^{3+} and $MPEG_{53}$-*b*-$P(NIPAAM)_{60}$-*b*-$P(MMA)_3-Eu^{3+}$ spectra. Moreover, in the presence of Au nanoparticles, the $^7F_2/^7F_1 \leftarrow {}^5D_1$ (≈543 nm) transition is bleached completely. This bleaching is associated with the large spectral overlap between the absorption spectrum of Au nanoparticles (the acceptor) and the emission spectrum of Eu^{3+} (the donor). From this spectral overlap it can be concluded that fluorescence resonance energy transfer (FRET) occurs in this system.[28] As the rate of FRET is dependent strongly on the distance *r* between acceptor and donor (D−A) and is proportional to r^{-6}, it can be concluded that the Eu^{3+} ions are located in the immediate vicinity of the Au−nanoparticle surfaces, in order for the $^7F_2/^7F_1 \leftarrow {}^5D_1$ (~543 nm) transition to vanish completely. The *m*/*e* ratio for this system (0.4; *cf.* Table 4) is dramatically different from what was found for the system with only Eu^{3+} and the $MPEG_{53}$-*b*-$P(NIPAAM)_{60}$-*b*-$P(MMA)_3-Eu^{3+}$ systems (1.6 and 1.3, respectively). Hence, it can be concluded that the chemical environment surrounding the Eu^{3+} ions is vastly different in the presence of Au nanoparticles. Specifically; the reduced emission from the $^7F_2 \leftarrow {}^5D_0$ transition indicates that Eu^{3+} has entered an environment with more C−H and O−H groups, which are efficient fluorescence quenchers. Thus, in the presence of $MPEG_{53}$-*b*-$P(NIPAAM)_{60}$-*b*-$P(MMA)_3$ and Au nanoparticles, Eu^{3+} resides very close to the colloidal Au core, as the $^7F_2/^7F_1 \leftarrow {}^5D_1$ (~543 nm)

TABLE 4. Magnetic to Electric Dipole (*m*/*e*) Transition Ratios from Steady-State Fluorescence Measurements for the Systems and Temperatures Indicated

	m/*e* (I_{591}/I_{615}) 25 °C	*m*/*e* (I_{591}/I_{615}) 50 °C
Eu^{3+}	1.6	1.6
$MPEG_{53}$-*b*-$P(NIPAAM)_{60}$-*b*-$P(MMA)_3-Eu^{3+}$	1.3	1.1
$MPEG_{53}$-*b*-$P(NIPAAM)_{60}$-*b*-$P(MMA)_3-Au-Eu^{3+}$	0.4	0.4
$P(NIPAAM)_{40}$-*b*-$P(SPMA)_5-Eu^{3+}$	1.8	1.3
$P(NIPAAM)_{40}$-*b*-$P(SPMA)_5-Au-Eu^{3+}$	0.4	0.4

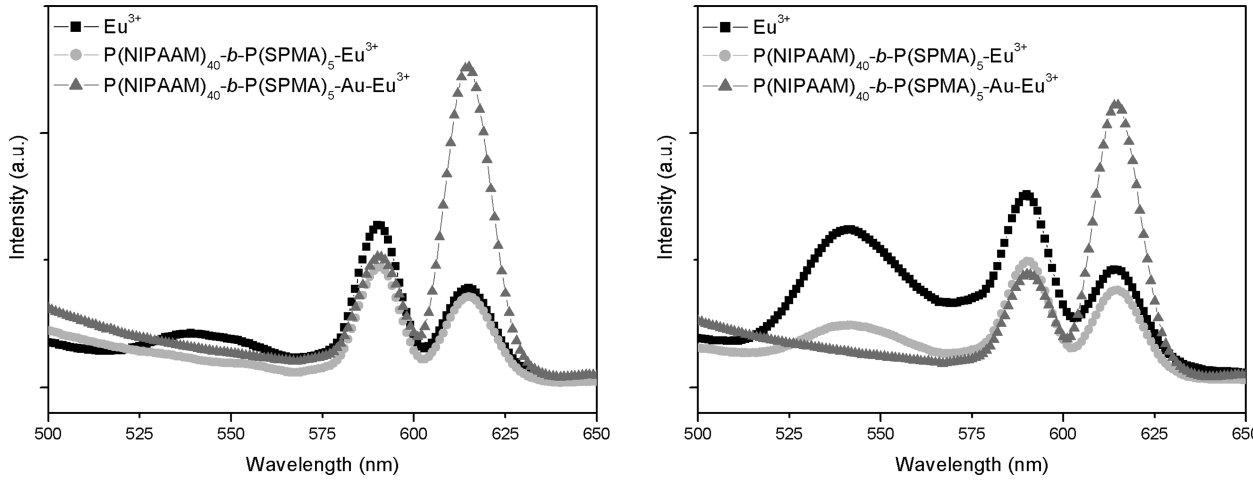

Figure 10. Steady-state fluorescence spectra for $EuCl_3$ and for the systems $P(NIPAAM)_{40}$-*b*-$P(SPMA)_5-Eu^{3+}$ and $P(NIPAAM)_{40}$-*b*-$P(SPMA)_5-Au-Eu^{3+}$ at two temperatures: 25 °C (left) and 50 °C (right). Excitation wavelength 405 nm.

band is quenched completely. Furthermore, Eu^{3+} enters a less polar environment since the relative intensities of the $^7F_1 \leftarrow {}^5D_0$ and $^7F_2 \leftarrow {}^5D_0$ transitions are reversed.[25] These findings point to Eu^{3+} either being intercalated within the polymer shell layer very close to the Au surface, or to Eu^{3+} interacting directly with Au *via* the citrate layer. From these results, mechanism (v) defined above, bathochromic shifts due to electron deficiency from a cation in close proximity to the Au nanoparticle, appears to be the most likely explanation for the shifts in the LSPR band of the $MPEG_{53}$-*b*-$P(NIPAAM)_{60}$-*b*-$P(MMA)_3-Au$ in the presence of Eu^{3+}.

Relative to only Eu^{3+} in bulk, the most distinctive feature in the systems containing Eu and the $P(NIPAAM)_{40}$-*b*-$P(SPMA)_5$ copolymer (*cf.* Figure 10 and Table 4) is that the *m*/*e*-ratio increases when polymer is introduced to the system, both at ambient and elevated temperatures. A likely explanation for this is that in the presence of the $P(NIPAAM)_{40}$-*b*-$P(SPMA)_5$ copolymer, the Eu^{3+} ions tend to associate preferentially with the sulfonate-containing block, and, as a result, they do not experience any change in polarity upon heating above the LCST. However, upon introduction of Au nanoparticles, Eu from the bulk can associate with the colloidal core, thus resulting in a reversal of the *m*/*e*-ratio (*cf.* Figure 10 and Table 4). The proximity of Eu^{3+} to the Au core is especially prominent when observing the spectra at 50 °C, where the $^7F_2/{}^7F_1 \leftarrow {}^5D_1$ (~543 nm) transition is completely bleached for $P(NIPAAM)_{40}$-*b*-$P(SPMA)_5-Au-Eu^{3+}$ as compared to systems without gold present. Above the LCST the polymer contracts, causing Eu^{3+} associated with the charged groups of the polymer to be in closer vicinity to the metal particle itself. A decrease in the *m*/*e* ratio is observed in $MPEG_{53}$-*b*-$P(NIPAAM)_{60}$-*b*-$P(MMA)_3$-based systems upon heating, going from 1.8 to 1.3 for $P(NIPAAM)_{40}$-*b*-$P(SPMA)_5-Eu^{3+}$. This is ascribed to the contraction of the polymer, causing the Eu^{3+} to enter the vicinity of the acrylamide block as water is being expelled from this environment. The fact that the *m*/*e* ratio stays constant at 0.4 in the presence of Au nanoparticles for both polymers and all temperatures studied here indicates that the Eu ions partition selectively close to the Au surface.

CONCLUSIONS

We studied the adsorption of a neutral triblock ($MPEG_{53}$-*b*-$P(NIPAAM)_{60}$-*b*-$P(MMA)_3$) and an anionic diblock ($P(NIPAAM)_{40}$-*b*-$P(SPMA)_5$) thermoresponsive copolymer onto Au nanoparticles and the resulting temperature-dependent optical properties of the polymer−Au constructs. Additionally, the temperature-dependent adsorption behavior of these amphiphilic block copolymers onto planar Au surfaces was probed using the quartz crystal microbalance with dissipation monitoring (QCM-D). On the basis of the QCM-D measurements, the negatively charged $P(NIPAAM)_{40}$-*b*-$P(SPMA)_5$ was found to form monolayers on gold both below and above the LCST, while the neutral $MPEG_{53}$-*b*-$P(NIPAAM)_{60}$-*b*-$P(MMA)_3$ copolymer adsorbed in the form of monolayers at low temperatures and multilayers above its lower critical solution temperature. This temperature-induced layer formation was taken advantage of and studied with DLS, UV, zeta-potential, and fluorescence measurements. Data from dynamic light scattering revealed the formation of $MPEG_{53}$-*b*-$P(NIPAAM)_{60}$-*b*-$P(MMA)_3-Au$ aggregates at high temperatures, while for $P(NIPAAM)_{40}$-*b*-$P(SPMA)_5-Au$ assemblies this was only observed when addition of Eu^{3+} allowed for a screening of the charges on the polymer. When the $MPEG_{53}$-*b*-$P(NIPAAM)_{60}$-*b*-$P(MMA)_3-Au$ system was subjected to a temperature ramping, UV−vis spectra exhibited a red shift in λ_{max} of the polymer−Au constructs. This phenomenon was explained within the framework of the Mie−Drude theory. It can be ascribed primarily to an increase in the refractive index of the passivating shell layer, caused by contraction of

the polymer structures; thus forming a denser layer, together with an increase in the volume fraction of the polymer layer, attributed to multilayer formation of the $MPEG_{53}$-*b*-$P(NIPAAM)_{60}$-*b*-$P(MMA)_3$ polymer. The observed red-shifts were completely reversible by cooling of the samples. Experiments with added $EuCl_3$-salt to the polymer−Au conjugates caused precipitation, which was reversible upon agitation. We also demonstrated that Eu^{3+} was associated with the polymers both in the presence and absence of Au nanoparticles, as evidenced by a quenching of the Eu^{3+} fluorescence emission. For the Au nanoparticle-containing systems, Eu^{3+} was found to reside close to the Au surfaces, as indicated by the complete bleaching of the $^7F_2/^7F_1 \leftarrow {}^5D_1$ emission band, due to a Förster energy transfer between Eu^{3+} and the LSPR band of Au. The obtained results demonstrate that it is possible to tune adsorption and absorption features for polymer−nanoparticle constructs by the correct choice of passivating layers and through means of temperature control. These gold−polymer assemblies show how it is possible to utilize gold nanoparticles to assess changes in structural conformation and behavior of immobilized macromolecules, whether it is caused by flocculation, plaque formation, or temperature- or other stimuli-induced changes in the adsorbed layer. This is of course highly dependent upon choice of passivating layer and other parameters such as environment and application, and would also enable studies of, for example, surface- or stimuli-induced unfolding of proteins on a plasmonic carrier. Plasmon-resonant gold nanoparticles with an adsorbed thermoresponsive polymer should be useful in biological labeling and to develop smart drug delivery systems.

MATERIALS AND EXPERIMENTAL METHODS

Materials and Synthesis and Characterization of Copolymers. Gold nanoparticles (30 nm in diameter) were purchased from Ted Pella, Inc. The various PNIPAAM-based block copolymers have been synthesized according to a slightly modified published procedure[29] *via* a simple "one-pot" atom transfer radical polymerization (ATRP). These include (methoxy-poly(ethyleneglycol)-*block*-poly(*N*-isopropylacrylamide)-*block*-poly(methyl methacrylate) ($MPEG_{53}$-*b*-$P(NIPAAM)_{60}$-*b*-$P(MMA)_3$) and poly(*N*-isopropylacrylamide)-*block*-poly(3-sulfopropyl methacrylate potassium) ($P(NIPAAM)_{40}$-*b*-$P(SPMA)_5$) (Figure 1)) The synthesis was carried out in water/DMF (40/60, v/v) solvent mixtures at 25 °C with the initiator/CuCl/$CuCl_2$/Me_6TREN as the initiator/catalyst system (MPEG-macroinitiator (MPEG-MI), MPEG precursor (M_n = 2000 Da) from Fluka for the preparation of the triblock copolymer ($MPEG_{53}$-*b*-$P(NIPAAM)_{60}$-*b*-$P(MMA)_3$). Freshly distilled ethyl 2-chloropronate (ECP) was employed as initiator for the synthesis of the diblock copolymer ($P(NIPAAM)_{40}$-*b*-$P(SPMA)_5$). The preparation and purification of these polymers was conducted under similar conditions as described previously.[30,31] The general reaction condition is that we kept the molar feed ratio of [NIPAAM] = 2 M, [NIPAAM]/[MMA]/[MPEG-MI]/[CuCl]/[$CuCl_2$]/[Me_6TREN] = 70/10/1/1/0.6/1.6 and [NIPAAM]/[SPMA]/[ECP]/[CuCl]/[$CuCl_2$]/[Me_6TREN] = 70/20/1/1/0.6/1.6 for the corresponding polymer. When the NIPAAM conversion had reached *ca.* 90% (after ~25 min a ^{1}H NMR analysis on 0.1 mL solution withdrawn from the reaction mixture indicated that *ca.* 90% of the NIPAAM had been polymerized (disappearance of vinyl signals at δ = 5.5−6.0 ppm)), a well degassed solution of MMA ([MMA]/[MPEG-MI] = 10/1) or SPMA ([SPMA]/[ECP] = 20/1) in a water/DMF (40/60, v/v) mixture was added quickly to the reaction mixture *via* a syringe under an atmosphere of argon. After 1 h, the polymerization was stopped by exposing it to air, diluted with water and further dialyzed, first against 0.1 N KCl and then against distilled water for several days using a dialysis membrane of regenerated cellulose with a molecular weight cutoff of 3500 Da. The white solid triblock copolymer $MPEG_{53}$-*b*-$P(NIPAAM)_{60}$-*b*-$P(MMA)_3$ and diblock copolymer $P(NIPAAM)_{40}$-*b*-$P(SPMA)_5$ were then finally isolated by lyophilization.

The chemical structure and composition of the triblock copolymer and the diblock copolymer were ascertained by their ^{1}H NMR spectra (*cf.* Figure 11) with a Bruker AVANCE DPX 300 NMR spectrometer (Bruker Biospin, Fällanden, Switzerland), operating at 300.13 MHz at 25.0 °C by using DMSO-d_6 or D_2O as the solvent. The number-average molecular weight and the unit numbers of *m*, *n*, and *o*, in $MPEG_m$-*b*-$P(NIPAAM)_n$-*b*-$P(MMA)_o$ were evaluated by comparing the integral area of the end-capped methoxyl proton peak (1) of MPEG (δ = 3.30 ppm), the methyne proton peak (6) of PNIPAAM (δ = 3.85 ppm) and the methyoxyl (10) of PMMA (δ = 3.6 ppm) obtained from its ^{1}H NMR spectrum (Figure 11A). The composition of the triblock copolymer is estimated to be *m*/*n*/*o* = 53/60/3 ($MPEG_{53}$-*b*-$P(NIPAAM)_{60}$-*b*-$P(MMA)_3$), based on our previous asymmetric flow field-flow fractionation (AFFFF) experiments that the number of repeating units of the ethylene glycol of MPEG-macroinitiator is 53.[30] Similarly, we can calculate the composition of the diblock copolymer to be *m*/*n* = 40/5 ($P(NIPAAM)_{40}$-*b*-$P(SPMA)_5$) by comparing the integral area of the methyne proton peak (7) of PNIPAAM (δ = 3.85 ppm), the methyoxyl (10) of PMMA (δ = 3.6 ppm) as well

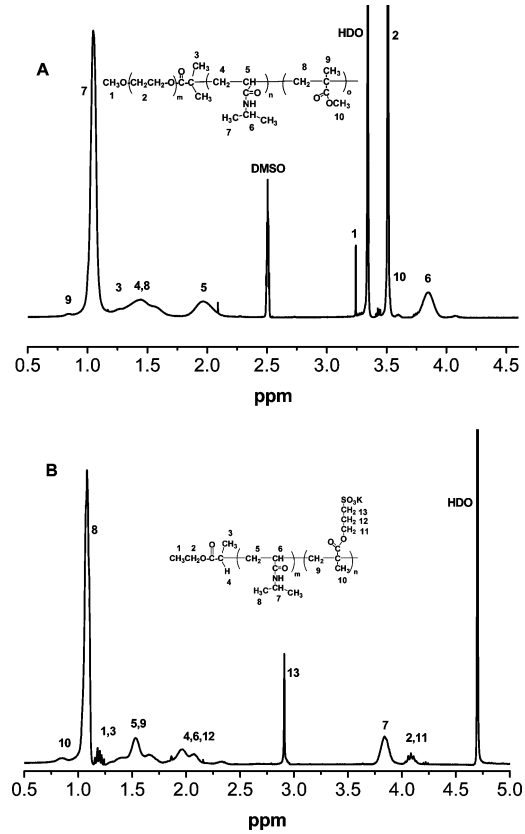

Figure 11. ^{1}H NMR spectra of synthesized triblock copolymer: $MPEG_{53}$-*b*-$P(NIPAAM)_{60}$-*b*-$P(MMA)_3$ (A, DMSO-d_6) and diblock copolymer: $P(NIPAAM)_{40}$-*b*-$P(SPMA)_5$ (B, D_2O).

as the ethyl isopropyl end group (1,3, $\delta = 1.2$ ppm) from its ^{1}H NMR spectrum (Figure 11B), and combining these results with the molecular weight from AFFFF.

Asymmetric Flow Field-Flow Fractionation. The asymmetric flow field-flow fractionation (AFFFF) experiments were conducted on an AF2000 FOCUS system (Postnova Analytics, Landsberg, Germany) equipped with an RI detector (PN3140, Postnova) and a multiangle (seven detectors in the range 35−145°) light scattering detector (PN3070, $\lambda = 635$ nm, Postnova). The $MPEG_{53}$-*b*-$P(NIPAAM)_{60}$-*b*-$P(MMA)_3$ samples (1.0 wt % in 0.01 M NaCl) were measured at ambient temperature (25 °C) using a 350 μm spacer, a regenerated cellulose membrane with a cutoff of 5000 (Z-MEM-AQU-426N, Postnova), and an injection volume of 20 μL. The measurements were performed by employing a constant detector flow rate of 1.0 mL/min. The focusing time was 5 min at a cross-flow of 4 mL/min. The cross-flow was then linearly reduced to zero during a period of time of 20 min. Processing of the measured data was achieved by the Postnova software (AF2000 Control, version 1.1.011). The molecular weight of the solutions was determined using this software with a random coil fit, and a refractive index increment (d*n*/d*c*) of 0.126 (determined by using the RI-detector at 32 °C). The $P(NIPAAM)_{40}$-*b*-$P(SPMA)_5$ sample (5.0 wt % in 0.01 M NaCl) was measured at 10 °C using a 500 μm spacer, a regenerated cellulose membrane with a cutoff of 1000 (Z-MEM-AQU-425N, Postnova), and an injection volume of 20 μL. The measurements were performed by employing a constant detector flow rate of 0.2 mL/min and a slot pump flow rate of 0.8 mL/min. The focusing time was 20 min at a cross-flow of 4 mL/min, and after the focusing time the cross-flow was kept constant for 10 min before it was linearly reduced to zero during a period of time of 5 min. The measured data were processed with the Postnova software (AF2000 Control, version 1.1.011). The molecular weight of the solutions was determined using this software with a Zimm fit, and a refractive index increment (d*n*/d*c*) of 0.152 (determined by using the RI-detector at 32 °C). Because of the strong associative nature of this polymer, the peaks resulting from the single polymer chains were very weak, resulting in a relative large error in the resulting molecular weights.

The polymer solutions were homogenized by stirring for 1 day before the gold nanoparticles were added or the planar gold surface was covered by the solution. For all experimental methods, except AFFFF, measurements were performed in 5 °C intervals in the temperature region 25−60 °C, following an equilibration period of ca. 15 min at each temperature, or 30 min of equilibration for the precipitation experiments with Eu.

Adsorption Protocol Au Nanoparticles. For studies of nanoparticle−polymer constructs, a typical polymer-adsorbing protocol consisted of adding a solution of the polymer (1 wt %, 0.5 mL) to 4.5 mL of the 30 nm Au nanoparticle solution ($2*10^{11}$ particles per ml). Samples were allowed to equilibrate for at least 24 h prior to analyses, yielding polymer−Au constructs, hereafter denoted as $MPEG_{53}$-*b*-$P(NIPAAM)_{60}$-*b*-$P(MMA)_3$−Au and $P(NIPAAM)_{40}$-*b*-$P(SPMA)_5$−Au. Approximately half of the samples were centrifuged and resuspended twice in ultrapurified water to remove excess polymer, the remaining 2.5 mL was kept as is. Additionally, experiments were performed where $EuCl_3$ (0.075 wt %, 0.5 mL) was added to 2 mL of the polymer−Au conjugates. Centrifugation was done at 14500 rpm for 10 min on a MiniSpinplus from Eppendorf AG, Germany.

QCM-D Measurements. Gold-coated quartz crystal microbalance (QCM) quartz crystals were acquired from KSV Instruments Ltd. QCM adsorption measurements were performed on a QCM-Z500 from KSV Instruments Ltd., in a direct deposition protocol wherein citrate-buffered (10 mM) solutions of the polymers (0.02 wt %) were added to the measuring chamber, followed by desorption in the citrate-buffer after equilibrium was attained. Cleaning of the Au crystals was done prior to measuring by immersing in a Piranha solution, consisting of H_2SO_4 (98%) and H_2O_2 (30%) in a 3:1 ratio, for ~20 min, followed by rinsing with ultrapurified water and drying under a stream of N_2-gas. All crystals were used immediately after preparation.

Turbidimetry. The turbidity experiments were performed on an NK60-CPA cloud point analyzer from phase Technology, Richmond, B.C., Canada. A detailed description of the equipment and determination of turbidities has previously been reported.[32] This instrument utilizes a scanning diffusive technique to probe phase changes of the solution with high sensitivity and accuracy. The light beam from an AlGaAs light source, operating at 654 nm, was focused on the measuring sample that was applied onto a special designed glass plate coated with a thin metallic layer of very high reflectivity (mirror). Directly above the sample, an optical system with a light-scattering detector continuously registers the scattered intensity signal (*S*) of the solution as it is subjected to a prescribed temperature alteration. The relation between the signal and the turbidity (τ) is given by the following empirical relationship $\tau\ (cm^{-1}) = 9.0 \times 10^{-9} S^{3.751}$.[32]

UV−Visible Spectroscopy. UV−vis spectra were recorded on a Shimadzu UV-2401PC instrument, equipped with a TCC-240 temperature control unit, over a wavelength range of 400−800 nm. The rate of precipitation of the $P(NIPAAM)_{40}$-*b*-$P(SPMA)_5$−Au−Eu^{3+} solutions was studied by time-resolved UV−vis experiments at two different temperatures, 25 and 60 °C, over a period of 2−4 days.

Fluorescence Measurements. Steady-state fluorescence measurements were performed on polymer−Eu, polymer−Au−Eu and pure Eu(III)Cl_3 solutions. Fluorescence experiments were conducted on a Fluorolog-3 from HORIBA Jobin Yvon apparatus, equipped with a Peltier element thermostat cell holder. Excitation wavelength was 405 nm.

Zeta-Potential Experiments. Zeta-potential measurements were conducted on a Nano-SZ zeta-sizer supplied from Malvern.

Dynamic Light Scattering Measurements. The dynamic light scattering (DLS) experiments were conducted with the aid of an ALV/CGS-8F multidetector version compact goniometer system, with 8 fiber-optical detection units, from ALV-GmbH., Langen, Germany. The beam from a Uniphase cylindrical 22 mW HeNe-laser, operating at a wavelength of 632.8 nm with vertically polarized light, was focused on the sample cell (10-mm NMR tubes, Wilmad Glass Co., 513−7PP-7) through a temperature-controlled cylindrical quartz container (with 2 plane-parallel windows), and the temperature constancy being controlled to within ±0.01 °C with a heating/cooling circulator, which is filled with a refractive index matching liquid (*cis*-decalin). The polymer solutions were filtered in an atmosphere of filtered air through a 5.0 μm filter (Millipore) directly into precleaned NMR tubes.

In the DLS measurements, the intensity correlation function was measured at eight scattering angles simultaneously in the range 22−141° with 4 ALV5000/E multiple-τ digital correlators. In the dilute concentration regime probed in this study the scattered field obeys Gaussian statistics. The measured correlation function $g^2(q,t)$, where $q = (4\pi n/\lambda)\sin(\theta/2)$, with λ, θ, and n being the wavelength of the incident light in a vacuum, scattering angle, and refractive index of the medium, respectively, can be related to the theoretically amenable first-order electric field correlation function $g^1(q,t)$ by the Siegert relationship $g^2(q,t) = 1 + B|g^1(q,t)|^2$, where B is usually treated as an empirical factor.

For suspensions containing particles of different size, the nonexponential behavior of the autocorrelation function can be portrayed by using a Kohlrausch−Williams−Watts[33,34] stretched exponential function. This procedure has been reported to be powerful in the analysis of correlation functions obtained from various colloid systems.[35−38] This approach is also successful to describe the correlation function data for the colloidal particles with adsorbed polymer studied in this work, and the algorithm employed in the analysis of the present correlation function data can be cast in the following form:

$$g^1(t) = \exp[-(t/\tau_{fe})^{\beta}] \quad (1)$$

where τ_{fe} is some effective relaxation time and β ($0 < \beta \leq 1$) is a measure of the width of the distribution of relaxation times. The high values of β ($\beta \geq 0.8$) observed for the present colloid particles at all conditions suggest that the size distribution of particles is narrow and the particles are nearly monodisperse. The mean relaxation time is given by

$$\tau_f = (\tau_{fe}/\beta)\Gamma(1/\beta) \quad (2)$$

where $\Gamma(1/\beta)$ is the gamma function.

The correlation functions were analyzed by using a nonlinear fitting algorithm (a modified Levenberg−Marquardt method) to attain best-fit values of the parameters τ_{fe} and β appearing on the right-hand side of eq 1. A fit was considered to be satisfactory if there were no systematic deviations in the plot of the residuals of the fitted curve and the values of the residuals were small. For 0.082 wt % solutions of $MPEG_{53}$-*b*-$P(NIPAAM)_{60}$-*b*-$P(MMA)_3$ in water and for $MPEG_{53}$-*b*-$P(NIPAAM)_{60}$-*b*-$P(MMA)_3-Eu^{3+}$ without Au nanoparticles in the interval 25−35 °C, the correlation functions were described by the sum of a single and a stretched exponential. Both modes are diffusive, and the fast mode depicts the behavior of unimers and micelles, whereas the slow mode illustrates the diffusion of intermicellar structures. At higher temperatures, the larger complexes dominate the decay of the relaxation process for $MPEG_{53}$-*b*-$P(NIPAAM)_{60}$-*b*-$P(MMA)_3-Eu^{3+}$, and this is described by the slow mode.

Since the relaxation mode always is diffusive ($D = 1/(\tau_f q^2)$) for these systems, the apparent hydrodynamic radii R_h of the particles can be calculated by using the Stokes−Einstein relationship

$$R_h = \frac{k_B T}{6\pi\eta D} \quad (3)$$

where k_B is the Boltzmann constant, T is the absolute temperature, η is the viscosity of the solvent, and D is the mutual diffusion coefficient. These suspensions become rather turbid at elevated temperatures, which may lead to problems with multiple scattering. However, at the conditions considered in this study we have only detected problems with multiple scattering at high temperatures for 0.082 wt % of $MPEG_{53}$-*b*-$P(NIPAAM)_{60}$-*b*-$P(MMA)_3$ in water.

Acknowledgment. This work has been made possible through funding from the Research Council of Norway within the FRINAT program, project no. 177556/V30.

Note added after ASAP publication: Due to production error, an uncorrected version of this article was published on January 15, 2010. The corrected version was reposted January 21, 2010.

REFERENCES AND NOTES

1. Shan, J.; Tenhu, H. Recent Advances in Polymer Protected Gold Nanoparticles: Synthesis, Properties and Applications. *Chem. Commun.* **2007**, 4580–4598.
2. Glomm, W. R. Functionalized Gold Nanoparticles for Applications in Bionanotechnology. *J. Disp. Sci. Technol.* **2005**, *26*, 389–414.
3. Shan, J.; Chen, H.; Nuopponen, M.; Viitala, T.; Jiang, H.; Peltonen, J.; Kauppinen, E.; Tenhu, H. Optical Properties of Thermally Responsive Amphiphilic Gold Nanoparticles Protected with Polymers. *Langmuir* **2006**, *22*, 794–801.
4. McConnell, W. P.; Novak, J. P.; Brousseau, L. C.; Fuierer, R. R.; Tenent, R. C.; Feldheim, D. L. Electronic and Optical Properties of Chemically Modified Metal Nanoparticles and Molecularly Bridged Nanoparticle Arrays. *J. Phys. Chem. B* **2000**, *104*, 8925–8930.
5. Cortie, M. New Uses for Gold in the Emerging Field of Nanotechnology. *Gold Bull.* **2003**, *36*, 74.
6. Galant, C.; Kjøniksen, A. L.; Knudsen, K. D.; Helgesen, G.; Lund, R.; Laukkanen, A.; Tenhu, H.; Nyström, B. Physical Properties of Aqueous Solutions of a Thermo-Responsive Neutral Copolymer and an Anionic Surfactant: Turbidity and Small-Angle Neutron Scattering Studies. *Langmuir* **2005**, *21*, 8010–8018.
7. Gil, E. S.; Hudson, S. A. Stimuli-Reponsive Polymers and Their Bioconjugates. *Prog. Polym. Sci.* **2004**, *29*, 1173–1222.
8. Kokufuta, E. Novel Applications for Stimulus-Sensitive Polymer Gels in the Preparation of Functional Immobilized Biocatalysts. *Adv. Polym. Sci.* **1993**, *110*, 157–177.
9. Malmsten, M. *Surfactants and Polymers in Drug Delivery*; Marcel Dekker, Inc.: New York, 2002; Vol. 122.
10. Prabaharan, M.; Mano, J. F. Stimuli-Responsive Hydrogels Based on Polysaccharides Incorporated with Thermo-Responsive Polymers as Novel Biomaterials. *Macromol. Biosci.* **2006**, *6*, 991–1008.
11. Rzaev, Z. M. O.; Dincer, S.; Piskin, E. Functional Copolymers of *N*-Isopropylacrylamide for Bioengineering Applications. *Prog. Polym. Sci.* **2007**, *32*, 534–595.
12. Ganta, S.; Devalapally, H.; Shahiwala, A.; Amiji, M. A Review of Stimuli-Responsive Nanocarriers for Drug and Gene Delivery. *J. Controlled Release* **2008**, *126*, 187–204.
13. Pissuwan, D.; Valenzuela, S. M.; Cortie, M. B. Therapeutic Possibilities of Plasmonically Heated Gold Nanoparticles. *Trends Biotechnol.* **2006**, *24*, 62–67.
14. Franzen, S. Surface Plasmon Polaritons and Screened Plasma Absorption in Indium Tin Oxide Compared to Silver and Gold. *J. Phys. Chem. C* **2008**, *112*, 6027–6032.
15. Mulvaney, P. Surface Plasmon Spectroscopy of Nanosized Metal Particles. *Langmuir* **1996**, *12*, 788–800.
16. Templeton, A. C.; Pietron, J. J.; Murray, R. W.; Mulvaney, P. Solvent Refractive Index and Core Charge Influences on the Surface Plasmon Absorbance of Alkanethiolate Monolayer-Protected Gold Clusters. *J. Phys. Chem. B* **2000**, *104*, 564–570.
17. Ung, T.; Giersig, M.; Dunstan, D.; Mulvaney, P. Spectroelectrochemistry of Colloidal Silver. *Langmuir* **1997**, *13*, 1773–1782.
18. Collier, C. P.; Saykally, R. J.; Shiang, J. J.; Henrichs, S. E.; Heath, J. R. Reversible Tuning of Silver Quantum Dot Monolayers Through the Metal-Insulator Transition. *Science* **1997**, *277*, 1978–1981.
19. Shiang, J. J.; Heath, J. R.; Collier, C. P.; Saykally, R. J. Cooperative Phenomena in Artificial Solids Made from Silver Quantum Dots: The Importance of Classical Coupling. *J. Phys. Chem. B* **1998**, *102*, 3425–3430.
20. Weast, R. C. *CRC Handbook of Chemistry and Physics*, 60th ed.; CRC Press, Inc.: Boca Raton, 1980.
21. LizMarzan, L. M.; Giersig, M.; Mulvaney, P. Synthesis of Nanosized Gold−Silica Core−Shell Particles. *Langmuir* **1996**, *12*, 4329–4335.
22. Malinsky, M. D.; Kelly, K. L.; Schatz, G. C.; Van Duyne, R. P. Chain Length Dependence and Sensing Capabilities of the Localized Surface Plasmon Resonance of Silver Nanoparticles Chemically Modified with Alkanethiol Self-Assembled Monolayers. *J. Am. Chem. Soc.* **2001**, *123*, 1471–1482.
23. Shan, J.; Nuopponen, M.; Jiang, H.; Viitala, T.; Kauppinen, E.; Kontturi, K.; Tenhu, H. Amphiphilic Gold Nanoparticles Grafted with Poly(*N*-isopropylacrylamide) and Polystyrene. *Macromolecules* **2005**, *38*, 2918–2926.
24. Kirby, A. F.; Richardson, F. S. Detailed Analysis of the Optical-Absorption and Emission-Spectra of Eu^{3+} in the Trigonal (C-3) $Eu(Dbm)_3 \cdot H_2O$ System. *J. Phys. Chem.* **1983**, *87*, 2544–2556.
25. Levy, D.; Reisfeld, R.; Avnir, D. Fluorescence of Europium(III) Trapped in Silica-Gel Glass as a Probe for Cation Binding and for Changes in Cage Symmetry During Gel Dehydration. *Chem. Phys. Lett.* **1984**, *109*, 593–597.
26. Matthews, L. R.; Knobbe, E. T. Luminescence Behavior of Europium Complexes in Sol-Gel Derived Host Materials. *Chem. Mater.* **1993**, *5*, 1697–1700.
27. Kirby, A. F.; Foster, D.; Richardson, F. S. Comparison of $^7F_J \leftarrow {}^5D_0$ Emission Spectra for Eu(III) in Crystalline Environments of Octahedral, near-Octahedral, and Trigonal Symmetry. *Chem. Phys. Lett.* **1983**, *95*, 507–512.
28. Lakowicz, J. R., *Principles of Fluorescence Spectroscopy*, 3rd ed.; Springer: New York, 2006.
29. Kjøniksen, A.-L.; Zhu, K.; Karlsson, G.; Nyström, B. Novel Transition Behavior in Aqueous Solutions of a Charged Thermoresponsive Triblock Copolymer. *Colloids Surf., A* **2009**, *333*, 32–45.
30. Zhu, K.; Jin, H.; Kjøniksen, A.-L.; Nyström, B. Anomalous Transition in Aqueous Solutions of a Thermoresponsive Amphiphilic Diblock Copolymer. *J. Phys. Chem. B* **2007**, *111*, 10862–10870.

31. Pamies, R.; Zhu, K. Z.; Kjøniksen, A.-L.; Nyström, B. Thermal Response of Low Molecular Weight Poly-(*N*-isopropylacrylamide) Polymers in Aqueous Solution. *Polym. Bull.* **2009**, *62*, 487–502.
32. Kjøniksen, A.-L.; Laukkanen, A.; Galant, C.; Knudsen, K. D.; Tenhu, H.; Nyström, B. Association in Aqueous Solutions of a Thermoresponsive PVCL-*g*-C11EO42 Copolymer. *Macromolecules* **2005**, *38*, 948–960.
33. Kohlrausch, R. *Pogg. Ann. Phys. Chem.* **1847**, 72.
34. Williams, G.; Watts, D. C. Non-symmetrical Dielectric Relaxation Behaviour Arising from a Simple Empirical Decay Function. *Trans. Faraday Soc.* **1970**, *66*, 80.
35. Ngai, K. L. Dynamics of Semidilute Solutions of Polymers and Associating Polymers. *Adv. Colloid Interface Sci.* **1996**, *64*, 1–43.
36. Phillies, G. D. J.; Lacroix, M. Probe Diffusion in Hydroxypropylcellulose−Water: Radius and Line-Shape Effects in the Solutionlike Regime. *J. Phys. Chem. B* **1997**, *101*, 39–47.
37. Phillies, G. D. J.; Richardson, C.; Quinlan, C. A.; Ren, S. Z. Transport in Intermediate and High Molecular Weight Hydroxypropylcellulose/Water Solutions. *Macromolecules* **2002**, *26*, 6849–6858.
38. Kjøniksen, A.-L.; Joabsson, F.; Thuresson, K.; Nyström, B. Salt-Induced Aggregation of Polystyrene Latex Particles in Aqueous Solutions of a Hydrophobically Modified Nonionic Cellulose Derivative and Its Unmodified Analogue. *J. Phys. Chem. B* **1999**, *103*, 9818–9825.